Towards the wind direction determination in RADARSAT-2 polarimetrie images

Francesco De Biasio & Stefano Zecchetto

Published online: 17 Feb 2017.

Submit your article to this journal 🗗

Towards the wind direction determination in RADARSAT-2 polarimetric images

Francesco De Biasio* and Stefano Zecchetto

Consiglio Nazionale delle Ricerche, Istituto di Scienze dell'Atmosfera e del Clima,
C.so Stati Uniti, 4, 35127 Padova
*Corresponding author, e-mail address: f.debiasio@isac.cnr.it

Abstract

The interpretation of SAR images of the sea surface is difficult, due to the complexity of the geophysics and of the interaction mechanisms between electromagnetic and sea waves. The determination of the wind direction is crucial for the evaluation of the wind speed, but its retrieval is still an open issue. One of the few methods able to extract the sea surface wind from SAR data only has been developed and extensively applied to Envisat ASAR images in the past years, using the two-dimensional wavelet transform to detect the backscatter signature related to locally coherent wind cells. A preliminary analysis on the applicability of this method to RADARSAT-2 fully polarimetric images has been conducted to verify if polarimetry may improve the detection of backscatter imprints related to the wind direction.

Keywords: SAR, polarimetry, sea wind, RADARSAT-2.

Introduction

Radar polarimetry has been extensively and successfully used for land features classification, land use and thematic mapping.

Applications of radar polarimetry on the ocean surface have been addressed to oil slick detection [Nunziata et al., 2011], oceanic circulation signature recognition [Ufermann and Romeiser, 1999] and sea ice monitoring [Schuechl et al., 2004], but relatively few attempts have been made in the field of sea surface winds.

Among them, Hwang et al. [2010], while confirming that co-polarized (co-pol) radar return has linear dependence on the wind speed, found also evidence that in cross-polarized (cross-pol) channels it exhibits a cubic dependence, due to breaking wave scatterers, which avoids saturation in high winds, thus opening the possibility to extend the wind speed measurement upper limit to higher winds than operational scatterometry currently allows.

Yueh et al. [2002], analyzing Ku-band multipolarization scatterometer data, found that the correlation coefficient between VV and HV polarization channels, as a function of the sea surface wind relative direction, has a peak-to-peak amplitude of about 0.4, and odd-symmetry. Conceivably, this would permit a complete recovery of the sea surface wind vector.

This contribution aims at a preliminary exploration of possible improvements of the wind direction assessment by using a wavelet transform analysis on RADARSAT-2 (RS2) polarimetric SAR images. The two-dimensional continuous wavelet transform (2DCWT) has already been applied to single look, VV-polarization Envisat ASAR wide swath images, as a tool to classify

the energy distribution of the radar backscatter in terms of spatial scales and position, and then to extract the direction of the local wind field from the backscatter pattern related to wind-aligned features [Zecchetto and De Biasio, 2002; 2008]. Although the application of this technique to SAR images involves issues not completely settled yet, the availability of different polarization views of the same backscatter scene may offer new insight in classifying the energy content in terms of different geophysical phenomena and spatial scales.

The polarimetric SAR quantities used in this study

The polarimetric radar backscattering measurables are usually represented by means of two equivalent description, namely the Polarimetric Covariance Matrix and the Polarimetric Coherence Matrix. The two representations express different linear combinations of the cross-products of the four complex S_{xy} $(x,y = H,V)$ elements of the Sinclair scattering matrix S, which models the scattering mechanism in terms of incident and scattered electromagnetic (EM) fields:

$$\begin{bmatrix} E_H^s \\ E_V^s \end{bmatrix} = \begin{bmatrix} S_{HH} & S_{HV} \\ S_{VH} & S_{VV} \end{bmatrix} \begin{bmatrix} E_H^i \\ E_V^i \end{bmatrix}. \quad [1]$$

In this notation the suffixes H,V indicate the component of the electromagnetic field polarization vector with respect to a Cartesian orthogonal frame of reference having the z axis in the travelling direction of the incident wave, the V component orthogonal to z and lying in the vertical plane, and the H component orthogonal to the other two. H and V directions reflect the orientation of the radar antennas. The paired H,V suffixes indicate the four possible combinations in which the EM wave is transmitted and received, and account for the polarization changes of the incident and scattered waves, while phase and intensity differences of the incident and scattered coherent EM waves are registered by the complex nature of the scattering matrix elements, which can be written in the form of an amplitude times a phase, e.g.:

$$S_{HH} = \Re(S_{HH}) + i\Im(S_{HH}) = |S_{HH}| \cdot e^{i\varphi} \quad [2]$$

where $\Re(S_{HH}), \Im(S_{HH})$ denote the real and imaginary part of the complex number S_{HH}, i represents the imaginary unit, $|S_{HH}|$ stands for the modulus of S_{HH} and φ for its phase.

The S_{HH} and S_{VV} channels are also called co-polarization channels, while S_{HV} and S_{VH} are called cross-polarized channels. In the monostatic case the reciprocity property states that $S_{HV} = S_{VH}$, so that the scattering matrix has only three independent complex elements and the Polarimetric Covariance and Coherency matrices are fully described by 3x3 matrices.

In this work we have adopted the Polarimetric Covariance Matrix representation C_{3L}, calculated through PolSARpro v. 4.1.5, a computational tool freely distributed by the European Space Agency. The Polarimetric Covariance Matrix is defined as:

$$C_{3L} = \begin{bmatrix} C_{11} & C_{12} & C_{13} \\ C_{21} & C_{22} & C_{23} \\ C_{31} & C_{32} & C_{33} \end{bmatrix} = \begin{bmatrix} <S_{HH}S_{HH}^*> & \sqrt{2}<S_{HH}S_{HV}^*> & <S_{HH}S_{VV}^*> \\ \sqrt{2}<S_{HV}S_{HH}^*> & 2<S_{HV}S_{HV}^*> & \sqrt{2}<S_{HV}S_{VV}^*> \\ <S_{VV}S_{HH}^*> & \sqrt{2}<S_{VV}S_{HV}^*> & <S_{VV}S_{VV}^*> \end{bmatrix} \quad [3]$$

where the symbol $<>$ means spatial ensemble averaging, and the asterisk '*' denotes complex conjugation. The C_{3L} matrix is Hermitian and thus has six independent complex elements that can be chosen in the upper half triangle of the matrix: (*HH,HH*), (*HH,HV*), (*HH,VV*), (*HV,HV*), (*HV,VV*) and (*VV,VV*). The self-adjointness implies also that the elements of the principal diagonal, (*HH,HH*), (*HV,HV*) and (*VV,VV*) are real. They are related to the total scattered power of the EM wave, and are indicated, for brevity, as *HH*, *HV* and *VV* respectively.

The test case SAR images

We use three Standard Quad-Polarization (SQ), Single Look Complex (SLC), RADARSAT-2 SAR (C-band, 5.405 GHz) images taken over the open sea.

Following the RS2 Product Description (document RN-SP-52-1238 online: http://gs.mdacorporation.com/products/sensor/radarsat2/RS2_Product_Description.pdf) the SLC SQ R2 images have nominal pixel spacing from 8.0 to 11.8 m in slant range and 5.1 m in azimuth, and nominal scene size of 25 km x 25 km; however the SAR images can be of different size both in range and azimuth.

RS2 SQ SLC SAR images bring all the four polarization elements of the scattering matrix *S*: S_{HH}, S_{VV}, S_{HV} and S_{VH}. Ensemble spatial averaging of the C_{3L} elements has been performed with a moving window of 7 x 7 pixels, roughly equivalent to 129 m (slant range) x 34 m (azimuth).

Table 1 reports the main characteristics of the images used in this study as well as the environmental conditions in the corresponding areas, derived from the European Centre for Medium-Range Weather Forecasts (ECMWF) global model analysis fields. The three images have extension of 37 km in azimuth and 27 km in range, and cover the same area in the Aegean Sea, some 70 km southeast of the island of Crete, as reported in Figure 1, where the geographic positions of the images and the corresponding wind fields derived from ECMWF analysis are shown.

Table 1 - RADARSAT-2 test case SAR images characteristics.

#	acquisition date time	centre lat centre lon	inc. angle near range far range	pass	ECMWF 2m mean air-sea temp. difference	ECMWF 10m mean wind speed	ECMWF 10m mean wind dir.
1	25/11/2010 04:13 UTC	34.3241°N 26.5837°E	39.28° 40.71°	desc.	-1.6°C	8.8 ms⁻¹	242°
2	27/11/2010 16:09 UTC	34.3248°N 26.5792°E	29.13° 30.87°	asc.	-0.7°C	7.6 ms⁻¹	181°
3	21/12/2010 16:09 UTC	34.3244°N 26.5777°E	29.13° 30.87°	asc.	-0.9°C	6.9 ms⁻¹	161°

For all the images, the wind blew from south at a moderate wind speed regime (7 to 9 ms⁻¹), and the stability conditions were lightly unstable ($T_{air} - T_{sea} < 0$). It is clear, however, that the ECMWF fields have a too coarse grid spacing (25 km x 25 km) to fully describe the environmental conditions in the 37 km x 27 km areas imaged by RS2.
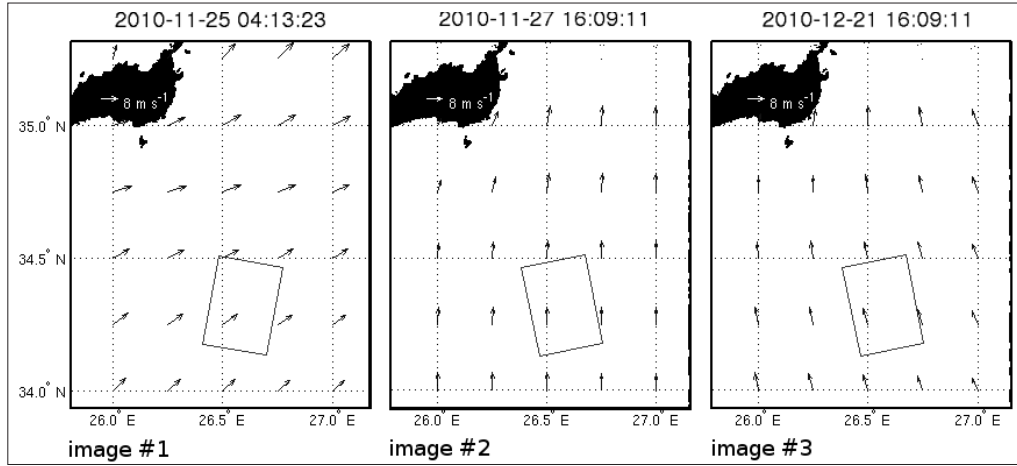
Figure 1 – Geographic position of the three SAR images, and collocated wind fields derived from ECMWF global model analysis.

Figure 2 top panels show the C_{33} (*VV*) elements of the Covariance Matrix, for the three images, while bottom panels report the C_{22} (*HV*) elements. We have chosen to show, in decibels and normalized to arbitrary units for sake of readability, only the *VV* and *HV* elements, which are respectively the polarization channels most and least sensitive to the wind.

Image #1 (Fig. 2, left) shows similar spatial structure of the radar backscatter both in *VV* and *HV* pol. The classical Fourier analysis performed along the mean wind direction reveals a wavelength peak of ≈ 2 km. Although the mottled appearance of the radar variability signature is suggestive of atmospheric convective turbulence, the low value of the air-sea temperature difference (-1.6°C) and the rather high mean wind speed (8.8 ms⁻¹) are unlikely to permit the formation of convective cells. We believe, instead, that such a spectral signature is probably the effect of the wind gustiness

$$G_u = \sigma_u / <u> \quad [4]$$

where σ_u is the standard deviation of the wind speed and $<u>$ the mean value. For a very gusty wind as the Adriatic Sea Bora, G_u ranges between 0.08 and 0.12 at $<u> \approx 8 \, \mathrm{ms}^{-1}$ with period of the order of minutes, as reported also by Grisogono and Belušić [2009]. Computation of a gustiness-like parameter from the image, i.e:

$$G_{\sigma_0} = \sigma_{\sigma_0} / <\sigma_0>\big|_{dB} \quad [5]$$

yields a value of 0.06 for *VV*, well compatible with the wind gustiness at this wind speed regime, and with the assumption of the Taylor's hypothesis of frozen turbulence [Taylor, 1938], so that the advection of the turbulence field can be assumed to be due to the mean

flow. In this perspective, the observed spectral wavelength (2 km) of the radar backscatter, interpreted in terms of pulsation of a wind with mean speed of 8 ms^{-1}, gives a period of ≈ 4 minutes. Note that, for HV, $G_{\sigma_0} = 0.03$, as a consequence of the lower sensitivity of the HV pol to the wind speed.
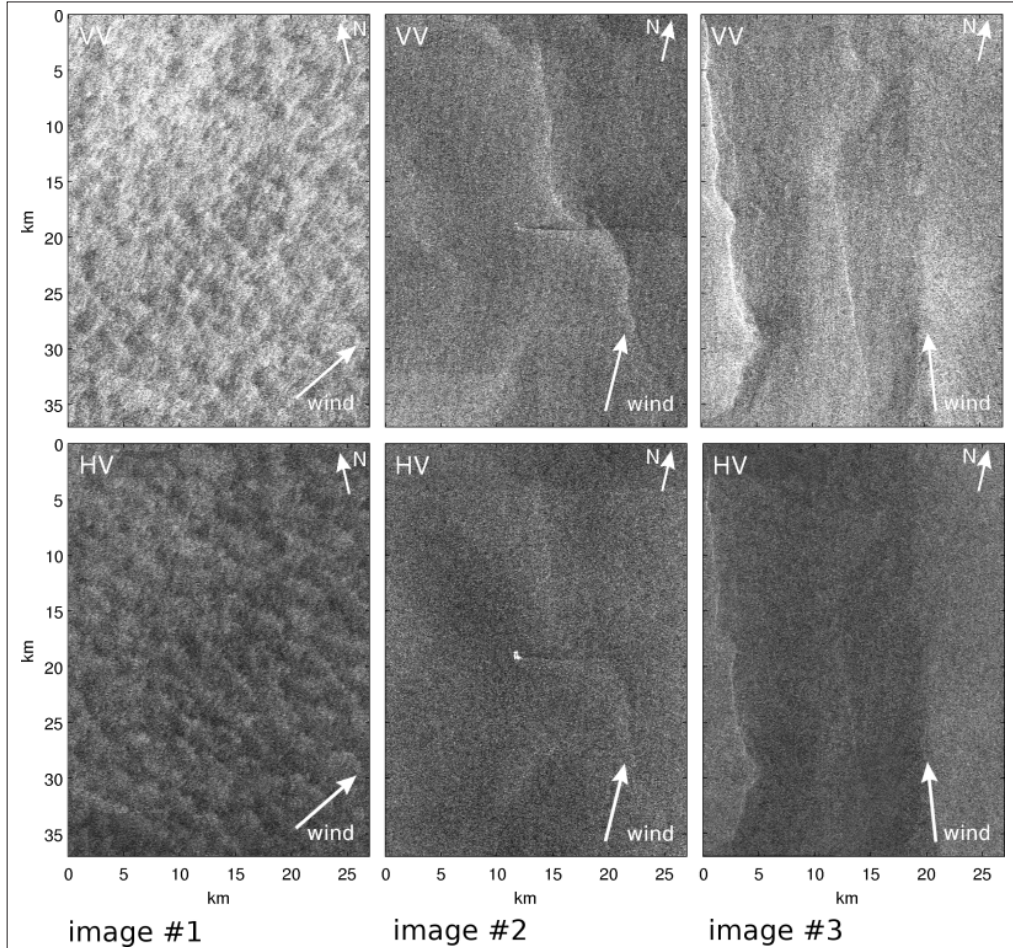
Figure 2 - The three test case SAR images *VV* (top panels) and *HV* (bottom panels) polarization channels. Each couple of *VV* and *HV* images, shown in decibels and normalized to their mean, have been independently equalized for sake of readability.

Images #2 and #3 (Fig. 2, centre and right) are characterized by a rather uniform, small scale background, modulated by mesoscale structures spanning the images vertically.

Image #2, which covers an area of relative uniform wind speed, is characterized only by few features at large scale: the mesoscale pattern is shown by both the co-pol and cross-pol channels, but in the latter it results attenuated. This is true also for the image #3, whose bounds encompass an area of strong longitudinal wind gradients. The large scale features

present in both the images #2 and #3 prevent a clear observation of the smaller scale features related to the wind cells.

The ECMWF air-sea temperature difference is unstable/neutral, and the ECMWF wind speed results lower than that of image #1. Slightly darker and lighter backscatter strings, superimposed as a loose texture on the background, are visible in the *VV* channel of both the images. Their orientation is compatible with the ECMWF wind direction (reported in the top right corners in Figure 2).

Methodology of the 2DCWT analysis

The SAR images have been analyzed with the 2DCWT, described by Zecchetto and De Biasio [2002, 2008]. This methodology is able to extract the structure of wind-aligned radar backscatter cells in moderate-to-high wind conditions (>5 ms^{-1}). It decomposes the image linearly on a given base of oriented and scaled elementary details. The coefficients of the decomposition can be used to selectively reconstruct the image. In the 2DCWT methodology, the criterion followed is to use only those coefficients which weigh more: they identify a maximum in the wavelet variance map, a 2-D surface reporting the squared modulus of the coefficients, averaged over the whole image support, as a function of the horizontal and vertical spatial scales of detail. Its physical interpretation is similar to that of the 2-D Fourier power spectrum, as a function of the horizontal and vertical wavelengths, with the difference that the latter cannot strictly describe non-periodic, quasi-periodic or intermittent signals in terms of wave numbers.

Sometimes the maximum of the wavelet variance map results ill-defined: this is the case when small size, wind-aligned features are concurring with mesoscale processes, as for example atmospheric gravity waves and/or synoptic scale wind modulations. In this case a suitable filtering procedure should be adopted. Once the meso-scale signals have been filtered out, the wavelet variance map maximum position roughly indicates the size of the atmospheric phenomenon which most modulates, throughout the image, the underlying Bragg scattering due to the wind. Sometimes other geophysical disturbances have wavelengths similar to that of the coherent wind cell structures, so that a clean isolation of this signal becomes problematic, as explained in the next section.

As pointed out by Zecchetto et al., [2010], a suitable choice of the wavelet coefficients allows the reconstruction of the image at a detail level evidencing locally coherent, wind-related cells of radar return. These backscatter cells have horizontal dimensions ranging from 0.3 to 4.0 km, and generally prevail over other geophysical signatures in this scale range. The aliased wind direction is identified by the major axis of the elliptic cell.

Our study of polarimetric SAR focuses specifically on the first step of the 2DCWT methodology, the separation of the image wavelet transform coefficients related to the wind-related backscatter cells from the other coefficients, through the wavelet variance map: a step which is by far the most elusive of the whole 2DCWT methodology, which will not be applied in full here.

Application of the 2DCWT to polarimetric SAR

Relying the 2DCWT method only on energy considerations, we do not take into account polarimetric phase information, and focus instead on the intensity of the elements of the

Covariance matrix. Figure 3 reports the wavelet variance maps of the image #1 for the six independent polarization elements of the Covariance Matrix, in log-log representation, as a function of the horizontal (along the image columns) and vertical (along the image rows) spatial scales, S_C and S_R. We have used 21 logarithmically-spaced scales on both directions, ranging from 200 m to 13 km.

The maximum of the wavelet variance map is found at about 3 km on the horizontal scale and 2 km on the vertical scale. This corresponds to the mottled roughness pattern visible in Figure 2, left panels, in the *VV* and *HV* channels. The other four channels are not shown in Fig. 2, but substantially account for the similar representation given by the wavelet variance maps of Figure 3.

The likeness of the six wavelet variance maps, yet giving a coherent interpretation of the image polarimetric content, prevents the straightforward extraction of information related to the direction of the surface wind vector, either considering each map alone, or simple linear combinations of two of them.
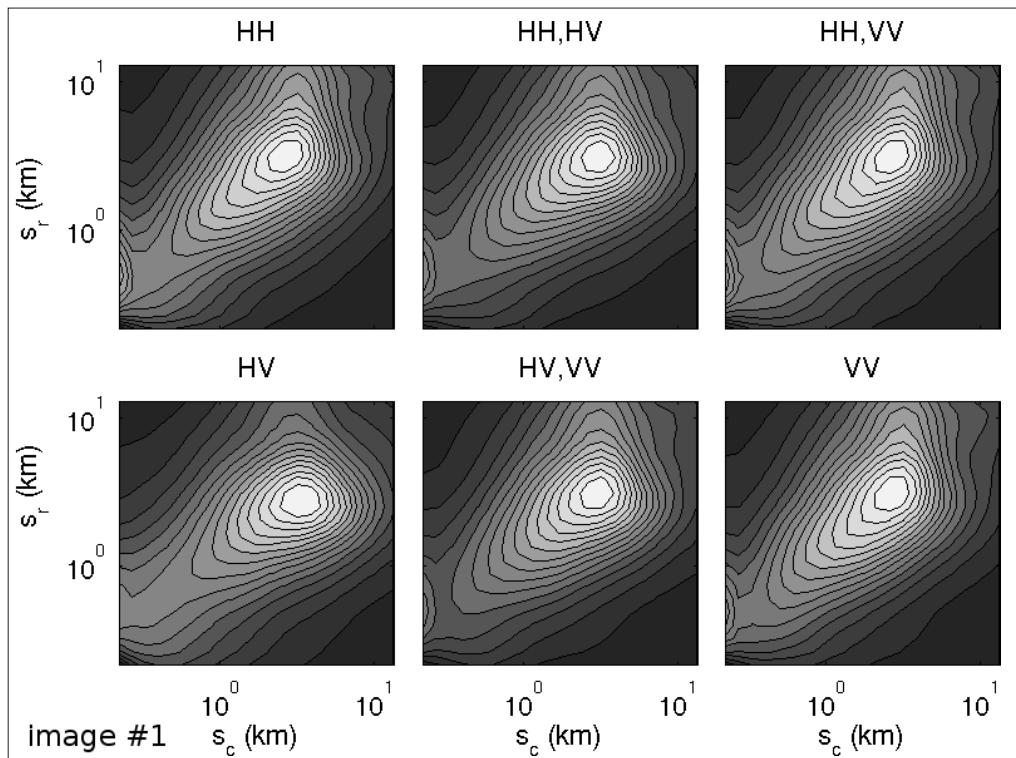

Figure 3 - Wavelet variance maps of the co- and cross-pol channels of R2 image #1.

The analysis of the wavelet variance maps of the image #2 is more encouraging. The co-pol and cross-pol variances (Fig. 4, bottom right and left respectively) reflect the structure of the patterns observed in the *VV* and *HV* channels (Fig. 2, centre panels): in the *HV* channel there is a maximum located towards the small scales, while in the *VV* channel there are two

maxima, the lower found at larger scales.

Multiple maxima are also found in the wavelet variance maps of the other four channels: they are visible, in Figure 4, at spatial scales corresponding to 0.5 km x 0.5 km and around 9.0 km x 13.0 km (partially cut out of the map).
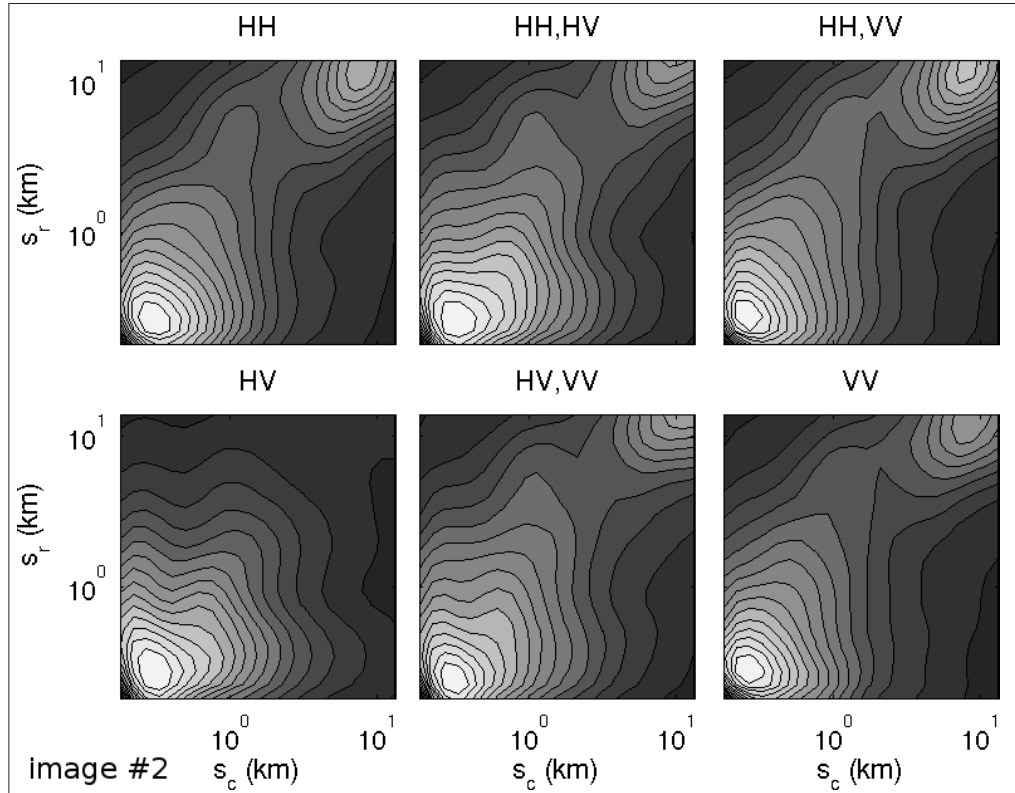

Figure 4 - Wavelet variance maps of the co- and cross-pol channels of R2 image #2.

The different situation depicted by the *HV* channel variance map with respect to all the others, guarantees the possibility of using such a difference to isolate the spectral peaks and discriminate geophysical signal of disparate spatial scales.

A similar representation is provided by the wavelet variance maps of SAR image #3 (Fig. 5), which pertains to geophysical conditions broadly equivalent to those of image #2. Moreover, the thermodynamic equilibrium conditions and the mean wind speed and direction, as derived from ECMWF analyses, turn out to be very similar.

In Figure 5 the presence of energy at low scales is witnessed by all the wavelet variance maps. Maxima of similar magnitude at larger scales are featured by all the maps but the HV channel.

This preliminary analysis confirms that the wavelet variance maps of the *HV* channel is less sensitive to large spatial scales features, where small scale, wind direction related backscatter structures do not leave any imprint. Cross-pol channels are then suitable

candidates to support the subsequent stages of the 2DCWT methodology.

Although this seems promising for the discrimination of wind direction related features from larger scale atmospheric and oceanic signatures present in the images #2 and #3, the wavelet variance maps of image #1 (Fig. 3) pose a serious limitation to the exploitation of the method. A maximum at scales of 2 to 3 km is present in all the channels of Figure 3, so that the wavelet variance maps are expected to represent the same geophysical process, which we have identified as expression of a gusty wind. Nonetheless, such a unvaried wavelet variance maps result poorly effective in the resolution of different energy maxima in terms of spatial scales.
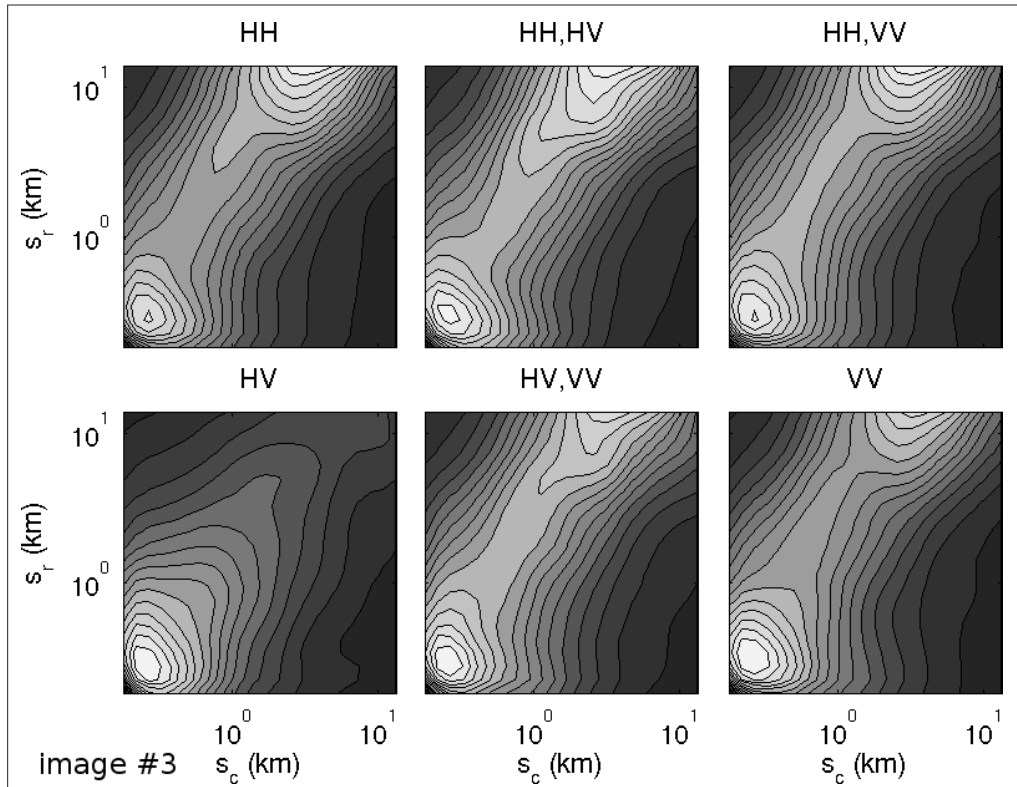

Figure 5 - Wavelet variance maps of the co- and cross-pol channels of R2 image #3.

Conclusions

As a follow up of the 2DCWT methodology of wind extraction from *VV*-pol Envisat ASAR WS SAR images, we have analyzed the possibilities offered by fully polarimetric RADARSAT-2 SAR Standard Quad Pol, Single Look Complex images.

We have applied the 2DCWT methodology to derive the wavelet variance maps, relative to the six independent channels of the Polarimetric Covariance Matrix C_{3L}, in three test cases, with the aim to improve the discrimination of wind direction related features from other

unwanted geophysical signals.

The analysis has revealed, in two cases, the possibility of using two different polarimetric channels, namely *VV* and *HV*, to filter out unwanted atmospheric and oceanic signals of different spatial size. Nonetheless, the first image of Figure 2 is characterized by a mottled signature with spectral peak wavelength of about 2 km, which is present in all the channels, preventing at the moment any effort to extract wind direction related features on the base of the wavelet energy/scale analysis.

Being this study still in a preliminary phase, there is not a complete understanding of how to perform signal filtering without destroying the geophysical signature of wind direction related structures. Some sort of image filtering, using linear combinations of co-pol and cross-pol channels, could maybe address the problem, because of the locality of the signal return present in the image, which is instead lost or hidden at the wavelet variance map level.

Acknowledgements

References

Grisogono B., Belušić D. (2009) - *A review of recent advances in understanding the meso- and microscale properties of the severe Bora wind,* Tellus, Vol. 61A, 1-16.

Hwang P.A., Zhang B. Perrie W. (2010) - *Depolarized radar return for breaking wave measurement and hurricane wind retrieval*. Geophys. Res. Lett., Vol. 37, No. L01604.

Nunziata F., Migliaccio M., Gambardella A. (2011) - Pedestal height for sea oil slick observation. IET Radar Sonar Navig., Vol. 5, No. 103.

Schuechl B., Flett D., Caves R., Cumming I. (2004) - *Potential of RADARSAT-2 data for operational sea ice monitoring*, Can. J. Remote Sens., Vol. 30, 448-461. doi: http://dx.doi.org/10.5589/m04-011.

Taylor G.I. (1938) - *The spectrum of turbulence.* Proc. R. Soc. London A, Vol. 164, 476-490. doi: http://dx.doi.org/10.1098/rspa.1938.0032.

Ufermann S., Romeiser R. (1999) - *A new interpretation of multifrequency / multipolarization radar signatures of the Gulf Stream front*. J. Geophys. Res., Vol. 104, No. C11, 25,697–25,705. doi: http://dx.doi.org/10.1029/1999JC900237.

Yueh S.H., Wilson W.J., Dinardo S. (2002) - *Polarimetric Radar Remote Sensing of Ocean Surface Wind.* IEEE Transactions on Geoscience and Remote Sensing, Vol. 40, No. 4: 793-800. doi: http://dx.doi.org/10.1109/TGRS.2002.1006350.

Zecchetto S., De Biasio, F. (2002) - *On shape, orientation and structure of atmospheric cells inside wind rolls in two SAR images.* IEEE Trans. of Geoscience and Remote Sensing, Vol. 40, No. 10, 2257-2262. doi: http://dx.doi.org/10.1109/TGRS.2002.803624.

Zecchetto S., De Biasio, F. (2008) - *A Wavelet Based Technique for Sea Wind Extraction from SAR Images*, IEEE Trans. of Geoscience and Remote Sensing, Vol. 46, No. 10, 2983-2989. doi: http://dx.doi.org/10.1109/TGRS.2008.920967.

Zecchetto S., De Biasio F., Miglietta M.M., Biamino W. (2010) - *Using SAR and LAM wind*

fields to investigate the effects of land/atmosphere interaction, Proceedings of the ESA Living Planet Symposium, June 28 – July 2, Bergen, Norway. ESA Special Publication SP-686. 2983-2989. doi: http://dx.doi.org/10.1109/TGRS.2008.920967.

Zecchetto S., De Biasio F., Miglietta M.M., Biamino W. (2010) - *Using SAR and LAM wind fields to investigate the effects of land/atmosphere interaction*, Proceedings of the ESA Living Planet Symposium, June 28 – July 2, Bergen, Norway. ESA Special Publication SP-686.